optica

High-resolution 3D refractive index microscopy of multiple-scattering samples from intensity images: supplementary material

SHWETADWIP CHOWDHURY,[1] MICHAEL CHEN,[1] REGINA ECKERT,[1] DAVID REN,[1] FAN WU,[2] NICOLE REPINA,[3] LAURA WALLER[1,*]

[1]Department of Electrical Engineering and Computer Sciences, University of California, Berkeley
[2]Department of Molecular and Cell Biology, University of California, Berkeley
[3]Department of Bioengineering, University of California, Berkeley
*Corresponding author: waller@berkeley.edu

Published 16 September 2019

This document provides supplementary information to "High-resolution 3D refractive index microscopy of multiple-scattering samples from intensity images," https://doi.org/10.1364/OPTICA.6.001211. We first show 3D refractive-index reconstruction of a simulated multiple-scattering phantom. We next describe the experimental preparation protocols used to prepare the biological samples visualized in the main text. We then detail the intuitive basis for the overlapping circles in Fourier spectra that occur when imaging a weakly scattering object, as used in our angle-calibration step. We follow with a demonstration of the importance of regularization in 3D computational reconstruction. We also describe the procedure used to register and blend together individual reconstructed volumes-of-interest to synthesize a final volume of the whole *C. elegans* worm. Lastly, we compare the reconstruction fidelities enabled by the multi-slice beam propagation (MSBP) method with those enabled by the 1st Born approximation. This comparison is conducted with the samples presented in the main text, to highlight that the MSBP method is uniquely suited for multiple-scattering biological samples.

1. Simulated reconstruction

We demonstrate our reconstruction algorithm for 3D refractive index recovery of a phantom simulation. The phantom was designed to mimic a highly-scattering spherical cell. The phantom's main body, nucleus, central nucleolus, and interspersed vesicles had refractive indices of 1.4, 1.38, 1.45, and 1.52, respectively. The surrounding media had refractive index of 1.33, to mimic water. The differences in refractive index within this cell are sufficiently large so that the cell is not a weakly-scattering sample – thus, reconstruction methods based on the 1st Born scattering model cannot be reliably used.

In Fig. S1, we demonstrate the reconstruction fidelity obtained by the multi-slice beam-propagation (MSBP) framework introduced in the main text. Fig. S1(a,b) show the true lateral (x-y) and axial (x-z) cross-sectional planes through the sample's volume, respectively. Fig. S1(c,d) shows the corresponding MSBP-reconstructed lateral and axial planes. We observe that both the lateral and axial cross-sectional planes through the MSBP reconstructed volume show excellent matching with their corresponding planes through the volume of the true simulated

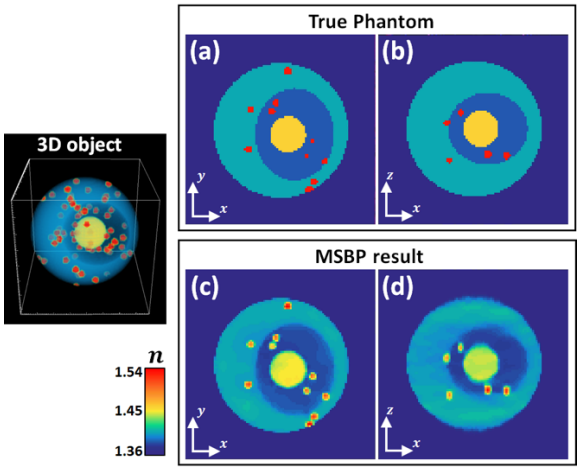

Fig. S1. Simulation results for 3D spherical cell phantom. (a,c) Lateral and (b,d) axial cross-sectional planes through the sample volume are shown for both the true phantom and the result reconstructed via our introduced framework, respectively.

phantom.

Because the MSBP reconstruction protocol relies on a nonlinear and nonconvex optimization framework, it is difficult to robustly study its accuracy and precision, which will ultimately be partially dependent on features within the sample (i.e., degrees of freedom within the reconstruction volume). However, this demonstration shows that high-fidelity 3D refractive-index reconstruction is possible and highly feasible in experimental settings.

2. Sample preparation

Preparation of 3T3 fibroblast cells

NIH 3T3 fibroblast cells were cultured in Dulbecco's Modified Eagle Medium (DMEM, Gibco) with 10% fetal bovine serum (FBS; Life Technologies) and 1% penicillin/streptomycin (P/S; Life Technologies) at 37 °C and 5% CO2. For imaging, glass coverslips (12mm diameter, No. 1 thickness; Carolina Biological Supply Co.) were coated with 10µg/mL human fibronectin (Millipore) for 30min at 37 °C. NIH 3T3 cells were passaged onto the coated glass coverslips, cultured for 24hr, and fixed with 3% paraformaldehyde for 20min. Fixed cells were mounted in phosphate buffered saline (PBS; Corning Cellgro) onto a second glass coverslip (24x50mm, No. 1 thickness; Fisher Scientific) and immobilized with sealant (Cytoseal 60; Thermo Scientific).

Preparation of *C. Elegans worms and embryos*

C. elegans embryos and worms were fixed with 2% formaldehyde for 1 minute, followed by a 10-minute freeze on dry ice. Fisherbrand microscope coverslips (22X40-1.5) were used to prepare the slides. Freeze-cracked slides were washed with PBS buffer twice. Then the samples were mounted within PBS buffer. Worms were generated under normal condition at 20°C. N2 strain was used in this study.

3. Symmetrically-shifted circles in intensity spectrum

In the main text, we note that the Fourier amplitude of an intensity measurement of a single scattering sample under angular illumination contains two distinct circles in Fourier space [1]. These two circles are symmetrically positioned in Fourier space around the origin. In our work, this phenomenon is important for two reasons: 1) it is a means to algorithmically calibrate an imaging system for its angular illuminations, and 2) it enables qualitative inspection of how much of a sample's scattering is due to single- vs multiple- scattering. In this section, we aim provide an intuition of where these two circles originate from as well as the relationship of their position to illumination angle.

In the case of weak scattering, the image at the camera plane is formed predominantly by single-scattering interactions within the sample. Thus, the image formation is linear in electric-field and its Fourier spectrum can be described by simple 2D operations. Given a certain operating wavelength (λ) and numerical aperture (NA) for the imaging system, the pupil function of the system is a DC-centered circle with radius of NA/λ in Fourier space. We simulate a noise-only sample with uniform spatial-frequencies, denoted by $x(\boldsymbol{r})$, where $\boldsymbol{r}$ is the 2D spatial vector. From Fourier optics, the electric-field at the image plane is given by $y(\boldsymbol{r}) = \mathcal{F}^{-1}\{p(\boldsymbol{k} - \boldsymbol{k_0}) \cdot \mathcal{F}\{x(\boldsymbol{r})\}\}$, where $\boldsymbol{k}$ is the 2D spatial-frequency vector, $\boldsymbol{k_0}$ is the 2D wave-vector for the illumination angle, $p(\boldsymbol{k})$ is the system's pupil function, and $\mathcal{F}\{.\}$ / $\mathcal{F}^{-1}\{.\}$ are the Fourier / inverse-Fourier operators [2]. The Fourier-spectra of the electric-field/intensity images are given by $Y(\boldsymbol{k}) = \mathcal{F}\{y(\boldsymbol{r})\}$ and $I(\boldsymbol{k}) = \mathcal{F}\{|y(\boldsymbol{r})|^2\}$, respectively.

In Fig. S2 below, we show how illumination angle (described by $\boldsymbol{k_0}$) affects the Fourier spectra of the image-plane's electric field and intensity, $Y(\boldsymbol{k})$ *and* $I(\boldsymbol{k})$, respectively. In all cases where the illumination angle lay within the imaging system's pupil function, $I(\boldsymbol{k})$ demonstrates a "brightfield" region in Fourier space composed of two symmetrically positioned circular regions [1]. The center-center distance between these two circular regions is set by the illumination angle, $2|\boldsymbol{k_0}|$. Furthermore, $I(\boldsymbol{k})$ also contains spatial-frequency information in Fourier space surrounding the "brightfield" regions. The visibility of the "brightfield" region compared to the surrounding region is set by the proportion of light that directly transmits through the sample. For example, in the case where the illumination angle lies outside the imaging system's pupil function (i.e., darkfield illumination, Fig. S2(d)), $I(\boldsymbol{k})$ does not demonstrate the two-circle "brightfield" region. In practice, illumination of a weakly-scattering biological sample results in a strong component of directly transmitted light. Thus, the corresponding $I(\boldsymbol{k})$ is visually dominated by only the "brightfield" components, as evidenced in the main text Figs. 1(c,e,g). However, in cases of multiple-scattering samples where the directly transmitted light is not the dominant imaging signal, the spatial-frequency signal from outside the "brightfield" regions in Fourier space also become apparent.

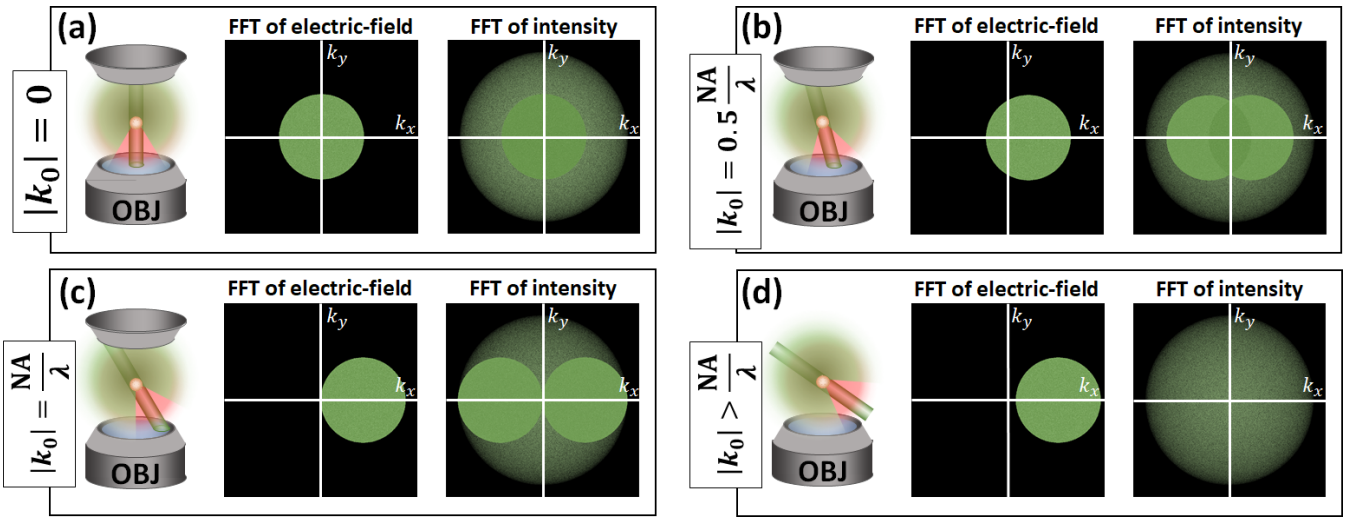

Fig. S2. Demonstrating the relationship between the Fourier amplitudes of the electric-field and intensity measurements, respectively, for **(a)** on-axis ($|\boldsymbol{k_0}| = 0$), **(b)** off-axis ($|\boldsymbol{k_0}| = 0.5\ NA/\lambda$), **(c)** off-axis ($|\boldsymbol{k_0}| = NA/\lambda$), and **(d)** darkfield ($|\boldsymbol{k_0}| > NA/\lambda$) illuminations.

4. Regularization for image reconstruction

In the reconstruction protocol outlined in our main text, we include a regularizer in step 9 to stabilize the nonlinear and nonconvex iterative convergence. Appropriate use of a regularizer is essential for high-fidelity optimization-based reconstructions and has two main functions: 1) to stabilize the convergence of the non-linear iterative solver in the presence of data noise. Noise, if unaccounted for, can cause overfitting in the iterative solver and lead to severe degradations in the reconstruction. 2) To enable good reconstruction in the case of poor conditioning. Being robust to poorly conditioned formulations is an important consideration because it is physically unfeasible to collect as many acquisitions as there are unknown variables in the reconstruction volume (i.e., voxels). As a benchmark, our input datasets for the 3D reconstructions presented in the main text contained ~4 times less data than the final 3D refractive-index reconstructions.

Hence, due to data noise and poor conditioning, the iterative solver traverses through a highly under-determined system with several local minima – the regularizer helps guide the solver towards a solution that satisfies some prior assumption. Our choice of using a 3D total-variation regularizer is appropriate in applications where the sample is assumed to be slowly-varying (or piece-wise constant) and where high-variation is attributed to noise [3].

However, careful consideration must be taken to not apply the regularizer too heavily. Doing so will enforce the regularizer's assumption too strongly and will lead to an overly biased reconstruction. Hence, the strength of the regularizer is often manually tuned to optimize reconstruction quality. In Fig. S3, we show lateral and axial cross-sectional planes from reconstruction volumes of the 3T3 fibroblast cell, obtained with over-regularization (Fig. S3(a,b)), proper regularization (Fig. S3(c,d)), and no regularization (Fig. S3(e,f)), respectively. We observe large high-contrast fringe artifacts corrupting the 3D reconstruction obtained by implementing no regularizer (indicated with yellow arrows in Fig. S3(e,f)). In contrast, excessive regularization overly biases the reconstruction against sample variation, and leads to a significant blurring-out of many of the fine details in the sample. Proper application of regularization, however, yields a reconstruction that retains sharp sample features and avoids unwanted artifacts.

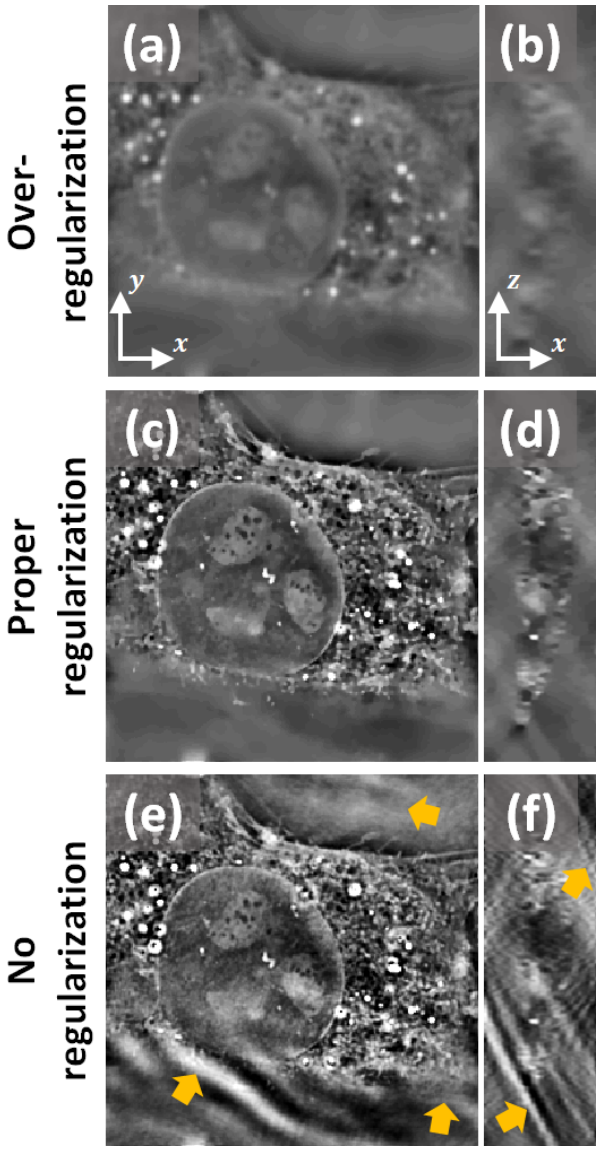

Fig. S3. Effects of regularization on image reconstruction fidelity. Lateral and axial cross-sectional planes from a 3D reconstructed volume of the 3T3 cell sample are shown after undergoing (a,b) over-regularization, (c,d) sufficient regularization, (e,f) and no regularization, respectively.

5. Total-volume synthesis from individual 3D reconstructed volumes within *C. elegans* worm

In the main text, we demonstrated 3D reconstruction of a whole *C. elegans* worm. Because the worm had a physical length greater than 1 mm, it could not be fully visualized within the imaging objective's FOV (~180 um diameter) – hence, we reconstruct 3D RI within a smaller volume-of-interest (VOI) at a time. Multiple VOIs spanning the whole worm were reconstructed by physically translating the worm. Here, we describe the procedure used to stitch together these separate VOIs into a complete 3D reconstruction of the whole worm.

Fourteen VOIs were required to span the whole *C. elegans* worm. Each individual VOI had dimensions 1200×1200×100 voxels, and had overlap with adjacent VOIs. The final synthesized RI volume of the whole worm had 1914×10408×118 voxels (2.3 total Gigavoxels). Fig. S4 illustrates the synthesis process of two individual volumes-of-interest (VOIs). This process is repeated for each subsequent VOI to synthesize together the final 3D reconstruction of the whole *C. elegans* worm, shown in the main text Fig. 5.

Fig. S4(a) shows the center depth slice from the first and second VOI. VOI1 captures the head of the worm and VOI2 captures the start of the worm's intestinal tract, with overlap (in this case, the overlap covers the worm's pharynx bulb). Standard 3D rigid-body registration algorithms [4] can identify this overlap and find the 3D translational difference between VOI1 and VOI2 (Fig. S4(b)). This translational difference was used to zero-pad both VOI1 and VOI2 to position them properly with respect to each other, within a greater synthesized volume. We designate the padded versions of VOI1 and VOI2 as VOIp1 and VOIp2 (Fig. S4(b)). At this point, VOIp1 and VOIp2 could in theory be simply averaged over the non-zero values to generate the synthesized volume – however, in practice, such averaging leads to edge-artifacts, as indicated by yellow arrows in Fig. S4(f).

To avoid such artifacts, we adopt a weighted-average scheme for combining VOIp1 and VOIp2. We first generate 3D masks for VOIp1 and VOIp2, designated as VOIm1 and VOIm2, respectively. These masks were initialized with values 1 in locations of all non-zero

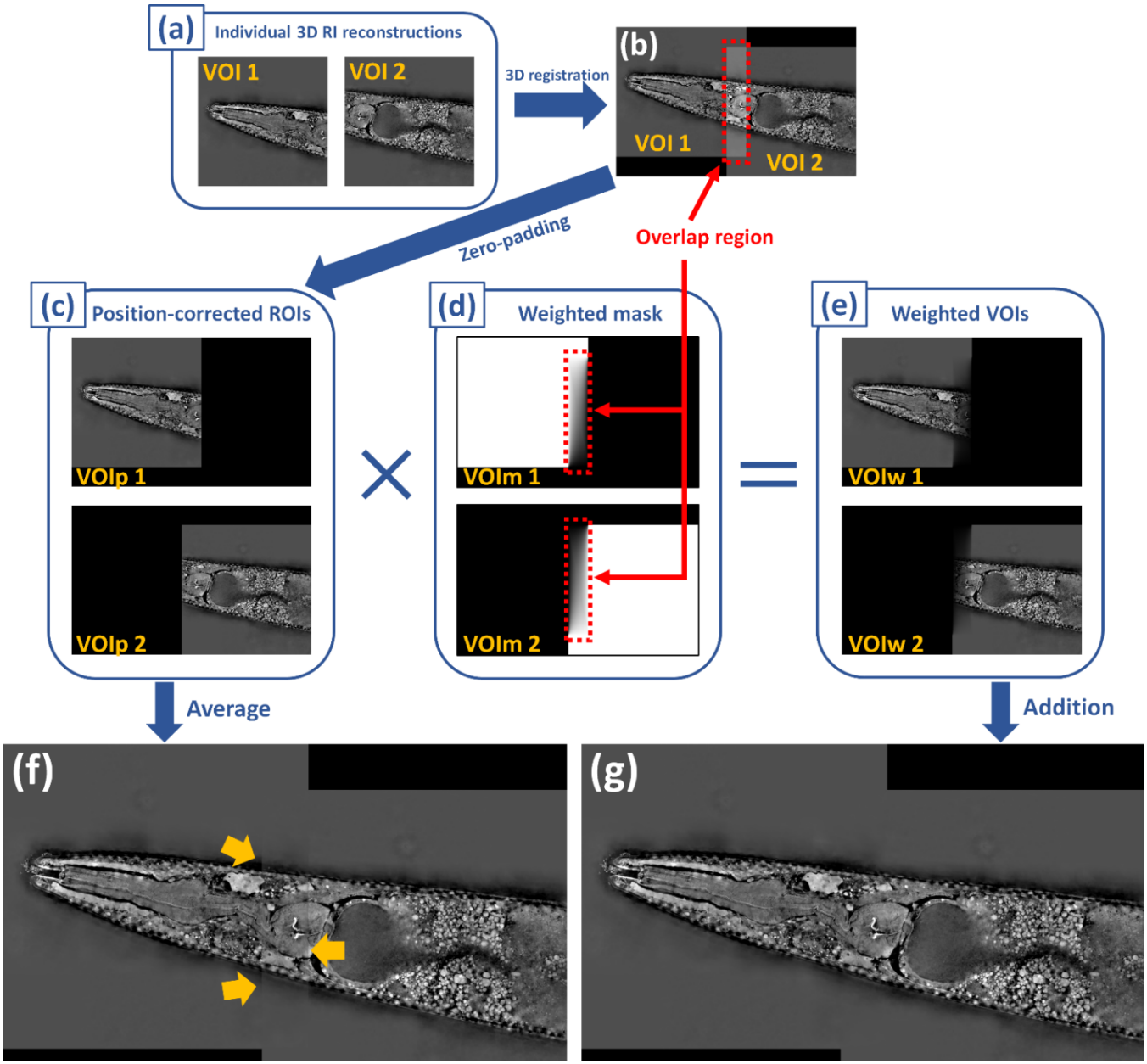

Fig. S4. Outline of how two reconstructed refractive index (RI) volume patches are stitched together to form a larger RI volume. **(a)** Start with two adjacent volumes-of-interest (VOIs) that overlap to contain a set of the same sample features. **(b)** 3D rigid-body registration algorithms can identify the region of overlap to subsequently calculate the translational difference between VOI1and VOI2. **(c)** Appropriate zero-padding positions VOI1 and VOI2 properly with respect to each other, in a larger volume space. **(d)** 3D weighting masks are generated. The values within the overlap region (identified in (b)) are set via weighted-average. **(e)** Multiplication of the zero-padded VOIs and the weighted masks results in the weighted VOIs. **(f)** Standard averaging across the zero-padded VOIs results in a synthesized volume with edge artifacts (indicated with yellow arrows). **(g)** However, simple addition across the weighted VOIs results in a synthesize volume with no apparent edge artifacts.

values in VOIp1 and VOIp2, and zero elsewhere. Afterwards, the values of the masks within the overlap-region between VOI1 and VOI2, as identified earlier, were replaced by a normalized weighted average. This weighted average was calculated based on the distance of each point to the closest edge of the overlap-region consisting of all ones Fig. S4(d). This weighted average protocol is similar to what is often used in standard alpha-blending algorithms [5]. Afterwards, VOIp1 and VOIp2 were multiplied by VOIm1 and VOIm2, to result in the weighted VOIs, VOIw1 and VOIw2, respectively (Fig. S4(e)). A simple addition then results in the fully synthesized volume merging VOI1 and VOI2 (Fig. S4(g)). After comparing Fig. S4(f,g), we see that the weighted average protocol for volume synthesis appropriately avoids the edge artifacts that plague the volume synthesis via direct averaging.

6. Reconstruction comparison between 1st Born and multi-slice scattering models

Applying the 1st Born scattering assumption when reconstructing a sample's 3D refractive index (RI) is a popular strategy employed by many diffraction tomography techniques [6]. However, though this assumption is valid for weakly-scattering samples, many biological samples are multiple scattering and cannot be optically characterized by 1st Born scattering. In the main text, we investigated the multi-slice beam propagation (MSBP) model for the robust 3D RI reconstruction of weakly-scattering and multiple scattering biological samples. In Fig. S5, we compare these

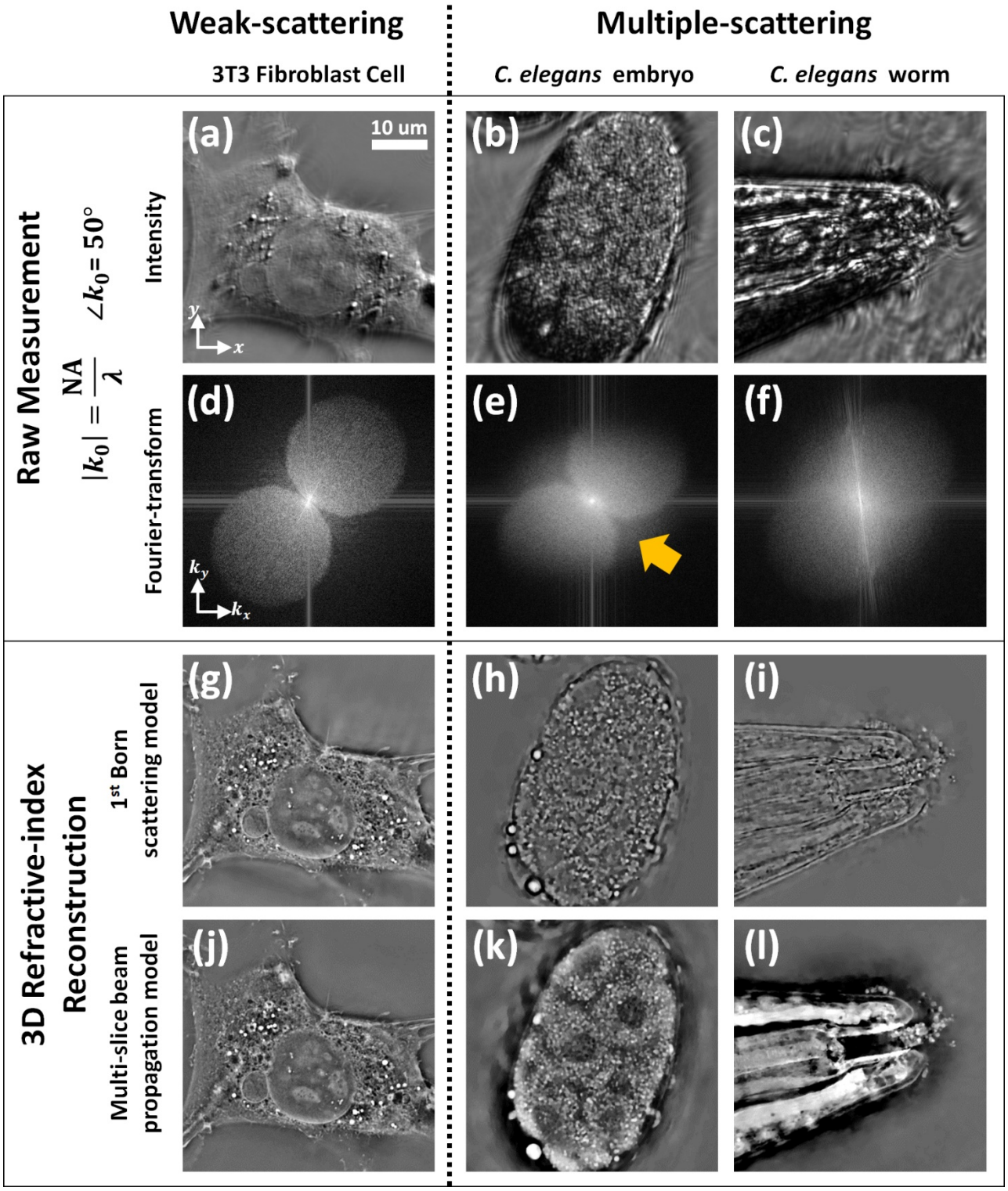

Fig. S5. 3D RI reconstruction fidelity comparing 1st Born with multi-slice beam propagation (MSBP) models. **(a,b,c)** Example raw acquisitions and **(d,e,f)** associated Fourier spectra from the datasets collected of the 3T3 fibroblast cell, *C. elegans* embryo, and *C. elegans* worm head, respectively. Samples with more multiple scattering have more energy outside the two circles defined by the illumination angle and NA. **(g,h,i)** The center cross-sectional plane of the 3D RI volumes of each reconstructed sample using the 1st Born model, as compared to **(j,k,l)** the multi-slice MSBP scattering model. Multi-slice accounts for multiple scattering, resulting in higher-quality RI reconstructions that better capture the low-frequency variations.

reconstructions with those obtained via the intensity-based 1st Born scattering inversion model [7]. We note that both models use the same raw data set – the difference between the reconstructions is due purely to which computational model was used.

In Fig. S5(a,b,c), we show an individual raw acquisition from the datasets acquired of the 3T3 fibroblast cell, *C. elegans* embryo, and *C. elegans* whole worm samples, respectively. Fig. S5(d,e,f) show their corresponding Fourier spectra. Recall that the 3T3 fibroblast cell is a weakly-scattering sample. This is confirmed by its Fourier spectra, which clearly demonstrates two "brightfield" circles symmetrically positioned in Fourier space. The *C. elegans* embryo is a multiple-scattering sample. This is also reflected in its Fourier

spectrum, which demonstrates significant signal outside the two-circle "brightfield" region (as indicated by yellow arrows in Fig. S5(e)). Finally, the *C. elegans* worm is also a multiple-scattering sample. Interestingly, its Fourier spectra shows virtually no distinct "brightfield" signal. This signifies that the *C. elegans* worm is an even stronger multiple-scattering sample than the *C. elegans* embryo.

Fig. S5(g,h,i) and Fig. S5(j,k,l) show the lateral cross-section through the center of the 3D RI volumes of the three samples, as reconstructed using the 1st Born and MSBP inversion models. Because the 3T3 fibroblast cell is a weakly-scattering sample, we expect the 1st Born assumption to be valid and to enable high-fidelity reconstruction. As expected, the reconstructed RI via 1st Born and MSBP match well (Fig. S5(g,j)). In the case of the multiple-scattering *C. elegans* embryo and worm samples, however, the reconstructions via the 1st Born (Fig. S5(h,i)) and MSBP Fig. S5(k,l)) scattering models show distinct and fundamental differences. 1st Born demonstrates an inability to reconstruct the lower spatial-frequencies in the presence of multiple-scattering, and essentially high-pass filters the RI content. This observation has been affirmed by previous works as well [8]. The degree of high-pass filtering is dependent on the degree of multiple-scattering within the sample, and the 1st Born RI reconstruction of the *C. elegans* worm (Fig. S5(i)) shows greater high-pass filtering than in that of the embryo (Fig. S5(h)). In both cases, important biological features that are easily visualized in the MSBP reconstruction, such as the individual cells within the embryo and the pharynx muscles and buccal cavity within the worm's head, cannot be visualized in the 1st Born reconstructions.

References

1. R. Eckert, Z. F. Phillips, and L. Waller, "Efficient illumination angle self-calibration in Fourier ptychography," Applied Optics **57**, 5434-5442 (2018).
2. J. W. Goodman, *Introduction to Fourier Optics* (Roberts and Company Publishers, 2005).
3. U. S. Kamilov, I. N. Papadopoulos, M. H. Shoreh, A. Goy, C. Vonesch, M. Unser, and D. Psaltis, "Optical tomographic image reconstruction based on beam propagation and sparse regularization," IEEE Transactions on Computational Imaging **2**, 59-70 (2016).
4. B. S. Reddy and B. N. Chatterji, "An FFT-based technique for translation, rotation, and scale-invariant image registration," IEEE Transactions on Image Processing **5**, 1266-1271 (1996).
5. T. Porter and T. Duff, "Compositing digital images," in *ACM Siggraph Computer Graphics*, (ACM, 1984), 253-259.
6. M. Born and E. Wolf, *Principles of Optics: Electromagnetic Theory of Propagation, Interference and Diffraction of Light* (CUP Archive, 2000).
7. R. Horstmeyer, J. Chung, X. Ou, G. Zheng, and C. Yang, "Diffraction tomography with Fourier ptychography," Optica **3**, 827-835 (2016).
8. Y. Sung, W. Choi, C. Fang-Yen, K. Badizadegan, R. R. Dasari, and M. S. Feld, "Optical diffraction tomography for high resolution live cell imaging," Optics Express **17**, 266-277 (2009).